Syringe injectable electronics

Jia Liu[#1], **Tian-Ming Fu**[#1], **Zengguang Cheng**[#1,2], **Guosong Hong**[1], **Tao Zhou**[1], **Lihua Jin**[3], **Madhavi Duvvuri**[1], **Zhe Jiang**[1], **Peter Kruskal**[1], **Chong Xie**[1], **Zhigang Suo**[3], **Ying Fang**[2], and **Charles M. Lieber**[1,3,*]

[1]Department of Chemistry and Chemical Biology, Harvard University, Cambridge, Massachusetts 02138, USA.

[2]National Center for Nanoscience and Technology, 11 Beiyitiao Street, Zhongguancun, Beijing 100190, P.R. China.

[3]School of Engineering and Applied Sciences, Harvard University, Cambridge, Massachusetts 02138, USA.

[#] These authors contributed equally to this work.

Abstract

Seamless and minimally-invasive three-dimensional (3D) interpenetration of electronics within artificial or natural structures could allow for continuous monitoring and manipulation of their properties. Flexible electronics provide a means for conforming electronics to non-planar surfaces, yet targeted delivery of flexible electronics to internal regions remains difficult. Here, we overcome this challenge by demonstrating syringe injection and subsequent unfolding of submicrometer-thick, centimeter-scale macroporous mesh electronics through needles with a diameter as small as 100 micrometers. Our results show that electronic components can be injected into man-made and biological cavities, as well as dense gels and tissue, with > 90% device yield. We demonstrate several applications of syringe injectable electronics as a general approach for interpenetrating flexible electronics with 3D structures, including (i) monitoring of internal mechanical strains in polymer cavities, (ii) tight integration and low chronic immunoreactivity with several distinct regions of the brain, and (iii) *in vivo* multiplexed neural recording. Moreover, syringe injection enables delivery of flexible electronics through a rigid shell, delivery of large volume flexible electronics that can fill internal cavities and co-injection of electronics with other materials into host structures, opening up unique applications for flexible electronics.

The emergence of flexible electronics has significantly extended the applications of electronics by allowing intimate interfaces between electronic units and non-planar surfaces for better monitoring and manipulation of their properties[1-3]. A variety of electronic devices[1-8] has been integrated on flexible and stretchable substrates to enable applications from foldable display to electronic skin[3-8]. 3D interpenetration of flexible electronics within existing structures could further broaden and open up new applications by directly interfacing devices with the internal structures of man-made and biological materials.

Recent work has shown that flexible electronics can be placed into 3D structures through surgical processes[9-12] or by being attached to and subsequently released from a rigid delivery substrates[13-14] for biological and biomedical applications. However, direct 3D interpenetration of electronics within these structures is limited by the intrinsic thin-film [14] supporting substrates. We have introduced a macroporous mesh paradigm that allow electronics to be combined, for example, with polymer precursors and cells to yield 3D interpenetration[15, 16], although controlled delivery and/or non-surgical placement of these ultraflexible open electronic networks into structures with seamless 3D integration and interpenetration has not been possible.

Here, we describe the design and demonstration of macroporous flexible mesh electronics that allow electronics to be precisely delivered into 3D structures by syringe injection and subsequently relax and interpenetrate within the internal space of man-made and biological materials. Distinct from previous reports[3, 17, 18], syringe injection requires complete release of the mesh electronics from a substrate so that the electronics can be driven by solution through a needle. The syringe injectable electronics concept involves (i) loading the mesh electronics into a syringe and needle, (ii) insertion of the needle into the material or internal cavity and initiation of mesh injection (Fig. 1a), (iii) simultaneous mesh injection and needle withdrawal to place the electronics through the targeted region (Fig. 1b), and (iv) delivery of the input/output (I/O) region of the mesh outside of the material (Fig. 1c) for subsequent bonding and measurements.

Design and implementation of electronics for syringe injection

The mechanical properties of the free-standing mesh electronics are important to the injection process. The basic mesh structure (Fig. 1d and Supplementary Fig. 1, a and b) consists of longitudinal polymer/metal/polymer elements, which function as interconnects between exposed electronic devices and I/O pads, and transverse polymer elements. The mesh longitudinal and transverse bending stiffness, D_L and D_T, are determined by the mesh unit cell and corresponding widths and thickness of the longitudinal and transverse elements, and the angle, a, [15, 16]. Simulations of D_T and D_L versus a (Fig. 1e) show that D_T (D_L) decreases (increases) for increasing a. Hence, increasing a facilitates bending along the transverse direction (reduced D_T) and should allow for rolling-up of the mesh electronics within a needle constriction, while at the same time increasing D_L, which should reduce bending and potential buckling along the injection direction.

The mesh electronics were fabricated, fully-released from substrates using reported methods[15, 16] and loaded into glass needles connected to a microinjector (details see,

Supplementary Information Sections 2 and 3 and Supplementary Figs. 2 and 3). Images of injection of a 2 mm wide sample through a 95 μm inner diameter (ID) glass needle show the compressed mesh ca. 250 μm from the needle opening (Fig. 1f), and then injected ca. 0.5 cm into 1x phosphate-buffered saline (PBS) solution (Fig. 1g), where the 3D image highlights the unfolding of the mesh structure from the point of the needle constriction (blue dashed box). Higher resolution images (Supplementary Fig. 4, a and b) show that the mesh structure is continuous as it unfolds. Similar results were obtained for injection of a 1.5 cm width sample through a 20 gauge (600 μm ID) metal needle (Supplementary Fig. 4c) demonstrating the generality of this injection through common glass and metal syringe needles.

To test further electrical continuity and functionality of the mesh electronics post-injection, we used anisotropic conductive film (ACF)[19] to connect the I/O pads of theelectronics post-injection to flexible cables that are interfaced to measurement electronics (Supplementary Fig. 5, a-d). Studies of the electrical performance and yield of devices following injection into 1x PBS solution through 100-600 μm ID needles (Fig. 1, i and j) highlight several points. First, metal electrochemical devices had an average device >94% and an average device impedance change, which represents an important characteristic for voltage sensing applications[20, 21], of <7% post injection (Fig. 1i). Second, silicon nanowire field-effect transistor (FET) devices had a yield > 90% for needle IDs from 260 to 600 μm, only dropped to 83% for the smallest 100 μm ID needles, and exhibited < 12% conductance change on average post injection (Fig. 1j). Together these results demonstrate the robustness of our mesh electronics design and the capability of maintaining good device performance following injection through a wide-range of needle IDs.

We have characterized the structures of different mesh electronics within glass needle-like constrictions to understand design parameters for successful injection (Fig. 2, a and b). Bright field microscopy images of mesh electronics with different structural parameters recorded from the central region of different ID glass channels (Fig. 2c) highlight two important features. First, mesh electronics with $\alpha = 45°$ and widths substantially larger than the constriction ID can be smoothly injected. Relatively straight longitudinal elements are seen in Fig. 2c, I and II, where the 5 mm 2D mesh widths are 11- and 20-times larger than the respective 450 and 250 μm ID needle constrictions. Second, even 1.5 cm width mesh electronics (Fig. 2c, III) can be injected smoothly through a 33-times smaller ID (450 μm) constriction.

The corresponding 3D reconstructed confocal images with higher resolution of $\alpha = 45°$ mesh electronics samples with mesh width/constriction ID ratios from 11 to 33 (Fig. 2d, I to III) highlight several important points. First, the longitudinal elements maintain a straight geometry without substantial bending through the constriction even for the 33:1 ratio (Fig. 2d, III). Second, these images show that the transverse element bend with a curvature that match the needle ID, and the longitudinal elements and estimated number of rolls of the mesh at the needle constriction are comparable to geometric calculations (see Supplementary Information Section 5.1). This latter point and further structural details can be seen in cross-sectional plots of these 3D images (Fig. 2e, I to III), which highlight uniformly organized transverse and longitudinal elements near the of the glass constriction

IDs. Third, there is no evidence for fracture of $\alpha = 45°$ design mesh elements. Indeed, simulations of the strain versus needle ID show that upper limit strain value for the mesh in a 100 μm ID needle, ~1%, is less than the calculated critical fracture strain (see Supplementary Information Section 5.2.3).

In contrast, bright-field and 3D confocal images recorded from injection of $\alpha = 0°$ mesh electronics (Fig. 2, c to e, IV) and thin-film electronics (Supplementary Fig. 6) show that these structures are not smoothly injected through the needle-like constrictions. Specifically, images of a mesh sample with $\alpha = 0°$ (Fig. 2d, IV) but smaller width than $\alpha = 45°$ (Fig. 2d, III) exhibit jammed mesh at the constriction. The structure is deformed and fills the cross-section of the channel (Fig. 2e, IV) versus rolling-up as observed for $\alpha = 45°$. Injection of thin film electronics with the same thickness and total width as the mesh in Fig. 2c, I for a width/needle ID ratio of 11 became jammed in the channel (Supplementary Fig. 6a, I). Reducing the thin film width/needle ID ratio to 4 did lead to successful injection (Supplementary Fig. 6a, II), although the 3D confocal microscopy images (Supplementary Fig. 6, b and c) show substantial buckling of the structure in contrast to our $\alpha = 45°$ mesh design. These results confirm that the reduced transverse bending stiffness for the $\alpha = 45°$ design plays a key role in allowing the mesh electronics to smoothly roll-up, follow the needle ID with minimum strain and thereby allow for injection of 2D widths > 30-times the needle ID.

Injection of electronics into man-made cavities and synthetic materials

We have investigated several applications of our syringe injectable electronics, including delivery of electronics to internal regions of man-made structures and live animals. First, mesh electronics, which incorporated addressable silicon nanowire piezoresistive strain sensors[16], were co-injected with polymer precursors through a small injection site (Fig. 3a, Supplementary Fig. 8a and Supplementary Information Section 3.5.1) into PDMS cavities, with I/O pads ejected outside the structure. Visual inspection, micro-computed tomography (μCT) images and photographs (Fig. 3b and Supplementary Fig. 8b) demonstrate that the mesh electronics unfolds and smoothly follows the internal cavity structure with continuous metal interconnects.

We monitored the response of the internal nanowire piezoresistive strain sensors as PDMS structures were deformed. A plot of strain recorded simultaneously from 4 typical calibrated devices (d1-d4, Fig. 3c) versus deformation with a point load along the z-axis shows compressive (d1, d3) and tensile (d2, d4) local strains recorded by the nanodevices. Mapping the strain response onto the optical image of the electronics/PDMS hybrid shows the nanowire sensors separated up to 4 mm (Supplementary Fig. 8c), where the compressive and tensile strains are consistent with expectation for the point-like deformation. These data suggest that syringe injection of mesh electronics with piezoresistive devices could be used to monitor and map internal strains within structural components with gaps/cracks in a manner not currently possible, and more generally, to simultaneously monitor corrosion and strain within internal cavities or cracks by using nanowire devices also to measure pH and other chemical changes[22].

Second, we investigated 3D gel structures without cavities as representative models of mesh electronics injection into soft materials and biological tissue. Images recorded versus time following injection mesh electronics into Matrigel™, a scaffold used in neural tissue engineering (Fig. 3, d to f)[23] shows that the mesh unfolds ca. 80% in the radial direction over a 3-week period at 37 °C. As expected, the degree of unfolding of the mesh electronics within the Matrigel™ depends on the gel concentration for fixed mesh mechanical properties (Fig. 3g) with ca. 90% and 30% unfolding for 25% and 100% Matrigel™, respectively. The ability to inject and observe partial unfolding of the electronics within gels with tissue-like properties also suggest that co-injection with other biomaterials[24] and/or cells[25] could be another application of injectable mesh electronics. Indeed, preliminary experiments show that co-injection of mesh electronics and embryonic rat hippocampal neurons into a Matrigel™ leads to 3D neural networks with neurites interpenetrating the mesh electronics (Supplementary Fig. 8, d and e). These co-injection results highlight potential opportunities for tissue engineering and stem cell therapy[25].

Injection of mesh electronics into brains of live animals

Last, we have investigated the behavior of mesh electronics stereotaxically injected into lateral ventricle (LV) and hippocampus (HIP) of live rodents (Fig. 4, a-d, and Supplementary Information Section 3.6)[26], where the capability of delivering millimeters width electronics through 100's μm outer diameter (OD) needles allows for a much smaller window in the skull than the width of electronics thereby reducing the invasiveness of surgery. Confocal microscopy images recorded from tissue slices from the LV region prepared 5 weeks post-injection of the mesh electronics (Fig. 4, e to g, Supplementary Fig. 9) demonstrate several important points. First, the mesh electronics relaxes from the initial ~200 μm injection diameter to bridge the caudoputamen (CPu) and lateral septal nucleus (LSD) regions that define the boundaries of the cavity in this slice (Fig. 4e). Second, higher-resolution images from boundary between the electronics and the CPu/subventricular zone (Fig. 4f and Supplementary Fig. 9a) show that mesh electronics interpenetrates with the boundary cells, and that cells stained with neuron marker NeuN associate tightly with the mesh. Third, control images recorded from the same tissue slice but opposite hemisphere without injected mesh electronics (Supplementary Fig. 9b, d-f) shows that the level of glial fibrillary acidic protein (GFAP) expression is similar with and without the injected mesh electronics, thus indicating little chronic tissue response to the mesh electronics. Fourth, images of the mesh electronics in the middle of LV (Fig. 4g and Supplementary Fig. 9c) show a large number of 4′, 6-diamidino-2-phenylindole (DAPI) stained cells bound to the mesh structure. These images indicate that (i) the mesh expands to integrate within the local extracellular matrix (i.e., the mesh is neurophilic), (ii) cells form tight junctions with the mesh, and (iii) neural cells migrate 100's of microns from the subventricular zone along the mesh structure[27]. Notably, these results suggest using injectable electronics to mobilize and monitor neural cells from the LV region to brain injury[28] and delivering mesh electronics to other biological cavities for recording and stimulation.

We also injected mesh electronics into the dense tissue of the HIP (Fig. 4d). Bright-field images of coronal tissues slices, prepared 5 weeks post-injection (Fig. 4h and Supplementary Fig. 10, a and b) demonstrate that the electronics is fully-extended in the

longitudinal direction. The mesh only relaxes a small amount with respect to the initial injection diameter (red dashed lines in Fig. 4h) given that the force to bend the mesh[16] is comparable to the force to deform the tissue[23, 29]. In addition, an overlay of bright-field and DAPI epi-fluorescence images (Fig. 4i) show that the injection did not disrupt the CA1 and dentate gyrus (DG) layers of this region. Notably, confocal images (Fig. 4j and Supplementary Figs. 10c, 11 and 12) highlight unique characteristics of the injectable mesh electronics in dense neural tissue. First, analysis of GFAP fluorescence shows that there is a limited or an absence of astrocyte proliferation near the mesh, although the full image (Fig. 4j) indicates a reduction in cell density at the central region of injection. Significantly, analysis of a similar horizontal slice samples prepared from three independent mesh injections (Supplementary Figs. 11, 12a, b), also show limited or absence of astrocyte proliferation around our electronics, and quantitative analyses (Supplementary Figs. 11b, II, 12b) demonstrate that GFAP values versus distance from and along the mesh electronics surface are similar to background level. Second, these images show healthy neurons (NeuN signal) surrounding and close to the SU-8 ribbons of the mesh (Fig. 4j, Supplementary Figs. 10c and 12c). Data and analyses from three independent samples (Supplementary Figs. 11 and 12d, I) support quantitatively this observation. Specifically, quantitative analyses (Supplementary Figs. 11b, I and 12d) demonstrate that the NeuN signals versus distance from and along the mesh electronics surface are enhanced or similar to background levels. These observations, which are similar to our results for injections into the LV show the capability of the mesh electronics to promote positive cellular interactions, and are distinct from the chronic response of neural tissue reported for insertion of silicon[30], metal[13], polyimide[31]/SU-8[32], and ultrasmall carbon[33] electrical probes that reduced neuron density and enhance astrocyte density near probes/tissue interface.

We attribute the unique biocompatibility syringe-injected mesh electronics to their ultrasmall bending stiffness and micrometer size features. The bending stiffness of injected mesh electronics (0.087 nN·m) is 4-6 orders of magnitude smaller than that of previous implantable electronics such as silicon (4.6×10^5 nN·m)[30, 34], carbon fiber (3.9×10^4 nN·m)[33] and thin-film electronic (0.16-1.3×10^4 nN·m)[12, 13, 35] probes (details, see Supplementary Information Section 5.2.2). The flexibility of the injected electronics is closer to the flexibility of tissue, which has been demonstrated to minimize mechanical trauma caused by motion between the probe and the surrounding tissue[33, 35]. In addition, the feature sizes of our injected mesh electronics, 5-20 μm, are the ≤single cells, which can also reduce chronic damage even when probe stiffness is much greater than tissue[33].

Last, we verified the capability of injected mesh electronics for recording brain activity in the HIP of anesthetized mice (Fig. 4, k and i; Supplementary Fig. 13). Representative multichannel recording using mesh electronics with Pt-metal electrodes (Fig. 4k) yielded well-defined signals in all 16 channels. The modulation amplitude, 200-400 μV, and dominant modulation frequency, 1-4 Hz, recorded are characteristic of δ-wave local field potentials (LFPs) in the anesthetized mouse. Moreover, spatiotemporal mapping of the LFP recordings (Supplementary Fig. 13d) reveals characteristic hippocampal field activity for the rodent brain[36, 37]. In addition, standard analysis (see Methods)[38, 39] of sharp downward spikes (Fig. 4l) show a uniform potential waveform with average duration of ca. 2 ms and peak-to-peak amplitude of ca. 70 μV characteristic of of single-unit action potentials[33]. In

the context of long-term chronic recording, our histology results and previous work[12, 13, 15] demonstrate biocompatibility and long-term stability of using SU-8 passivated interconnects, and long-term stability of metal oxide passivated silicon nanowire sensors[15, 40]. Hence, we believe these results together with the 'neurophilic' chronic response offer substantial promise for implantation and long-term brain activity mapping[41].

Conclusions

In summary, we have introduced a new strategy for delivery of electronics to the internal regions of 3D man-made and biological structures that involves syringe injection of submicron thickness, large-area macroporous mesh electronics. We have shown that mesh electronics with widths >30-times the needle ID can be injected and maintain a high yield of active electronic devices. *In-situ* imaging and modeling show that optimized transverse/ longitudinal stiffness enables the mesh to 'roll-up' passing through needle constrictions. We have demonstrated that injected mesh electronics with addressable piezoresistive devices are capable of monitoring internal mechanical strains within bulk structures, and also have shown that mesh electronics injected into the brains of mice exhibit little chronic immuno-reactivity, attractive interactions with neurons, and can reliably monitor brain activity. Compared to other delivery methods[9-18], our syringe injection approach allows delivery of large (with respect to injection opening) flexible electronics into cavities and existing synthetic materials through small injection site and relatively rigid shell. In the future, our new approach and results could be extended in several directions, including the incorporation of multifunctional electronic devices[7, 13, 16, 42] and/or wireless interfaces[13, 43] to further increase the complexity of the injected electronics. Additionally, recent reports[42, 44-46] have demonstrated that novel electrophysiological recordings enabled by nanoelectronic units require an intimate nanoelectronics-cellular interface. In this emerging direction, our syringe injectable electronics could serve as a unique yet general platform for building direct neuron-nanoelectronics interfaces for *in vivo* studies. Last, syringe injection brings the opportunity to co-inject mesh electronics with polymer precursor or cells into host systems for unique engineering and biomedical applications.

Methods

Freestanding injectable mesh electronics were fabricated on nickel relief layer as previously reported[15, 16]. Following release from the substrate, mesh electronics were modified by poly-D-lysine (MW 70,000 – 150,000, Sigma-Aldrich Corp.) and then loaded into syringe fitted with either a metal needle or a glass needle pulled by the commercial available pipette puller (Model P-97, Sutter Instrument). A microinjector (NPIPDES, ALA Scientific instruments Inc.) and manually controlled syringes (Pressure Control Glass Syringes, Cadence, Inc.) were used to inject electronics. 400 μm ID needle were used to investigate mesh electronics injection as a function of the fluid flow rate. Smooth mesh electronics injection can be established for flows from 20 – 150 mL/hr as long as the needle retraction speed matched the speed of the injected fluid. The lower limit for smooth injection, 20 mL/hr, is believed to be restricted by the smallest fluid drag force relative to the friction force between the rolled-up mesh electronics and the inner needle surfaces. The maximum flow, 150 mL/hr, was limited by the needle retraction speed of our set-up. To characterize

the structures of different mesh electronics within glass needle-like constrictions to understand design parameters for successful injection, a pulled glass tube with controlled ID central constriction is positioned under a microscope objective for bright-field and confocal fluorescence imaging, and the mesh electronics are injected partially through the constriction. Confocal microscopes (Olympus Fluoview FV1000 and Zeiss LSM 780 confocal microscope) were used to image the structure of the mesh electronics in glass channels and immunostained mouse brain slices. ACF (AC-4351Y, Hitachi Chemical Co.) bonding to the mesh electronics I/O was carried out using a home-made or commercial bonding system (Fineplacer Lambda Manual Sub-Micron Flip-Chip Bonder, Finetech, Inc.) with a flexible cable (FFC/FPC Jumper Cables PREMO-FLEX, Molex).

The PDMS cavity was designed with a step-like internal corrugation (4 steps, 0.1 cm drop/step, and projected cavity area of 2×4.8 cm^2). The strain response of silicon nanowire piezoresistive strain sensors was measured by a multi-channel current/voltage preamplifier (Model 1211, DL Instruments, Brooktondale, NY), filtered with a 3 kHz low pass filter (CyberAmp 380, Molecular Devices), and digitized at a 1 kHz sampling rate (AxonDigi1440A, Molecular Devices), with a 100 mV DC source bias voltage.

For *in vivo* brain recording from metal electrodes, in a typical procedure, a 100-200 μm ID glass needle loaded with mesh electronics, mounted in the stereotaxic apparatus and connected to a microinjector is positioned to a specific coordinate in the brain of an anesthetized mouse, and then the mesh is injected concomitantly with retraction of the needle so that the electronics is extended in the longitudinal (injection) direction. The flexible cable was connected to a 32-channel Intan RHD 2132 amplifier evaluation system (Intan Technologies LLC., Los Angeles, CA) with an Ag/AgCl electrode acting as the reference. A 20 kHz sampling rate and 60 Hz notch were used during acute recording. 300-6000 Hz bandpass filter[38] and spike-sorting algorithm[39] are used for single-unit action potential data analysis.

Supplementary Material

Refer to Web version on PubMed Central for supplementary material.

Acknowledgements

References

1. Kaltenbrunner M, et al. An ultra-lightweight design for imperceptible plastic electronics. Nature. 2013; 499:458–463. [PubMed: 23887430]

2. Timko BP, et al. Electrical recording from hearts with flexible nanowire device arrays. Nano Lett. 2009; 9:914–918. [PubMed: 19170614]

3. Kim D, et al. Epidermal electronics. Science. 2011; 333:838–843. [PubMed: 21836009]

4. Wang C, et al. User-interactive electronic skin for instantaneous pressure visualization. Nature Mater. 2013; 12:899–904. [PubMed: 23872732]

5. Tee BCK, Wang C, Allen R, Bao Z. An electrically and mechanically self-healing composite with pressure- and flexion-sensitive properties for electronic skin applications. Nature Nanotech. 2012; 7:825–832.

6. Takei K, et al. Nanowire active-matrix circuitry for low-voltage macroscale artificial skin. Nature Mater. 2010; 9:821–826. [PubMed: 20835235]

7. Mannoor MS, et al. Graphene-based wireless bacteria detection on tooth enamel. Nature Commun. 2012; 3:763. [PubMed: 22453836]

8. Sekitani T, et al. A rubberlike stretchable active matrix using elastic conductors. Science. 2008; 321:1468–1472. [PubMed: 18687922]

9. Mathieson K, et al. Photovoltaic retinal prosthesis with high pixel density. Nature Photon. 2012; 6:391–397.

10. Mandel Y, et al. Cortical responses elicited by photovoltaic subretinal prostheses exhibit similarities to visually evoked potentials. Nature Commun. 2013; 4:1980. [PubMed: 23778557]

11. Kim D, et al. Materials for multifunctional balloon catheters with capabilities in cardiac electrophysiological mapping and ablation therapy. Nature Mater. 2011; 10:316–323. [PubMed: 21378969]

12. Rousche PJ, et al. Flexible polyimide-based intracortical electrode arrays with bioactive capability. IEEE Trans. Biomed. Eng. 2001; 48:361–371. [PubMed: 11327505]

13. Kim T, et al. Injectable, cellular-scale optoelectronics with applications for wireless optogenetics. Science. 2013; 340:211–216. [PubMed: 23580530]

14. Kane MJ, Breen PP, Quondamatteo F, Olaighin G. BION microstimulators: A case study in the engineering of an electronic implantable medical device. Med. Eng. Phy. 2011; 33:7–16.

15. Tian B, et al. Macroporous nanowire nanoelectronic scaffolds for synthetic tissues. Nature Mater. 2012; 11:986–994. [PubMed: 22922448]

16. Liu J, et al. Multifunctional three-dimensional macroporous nanoelectronic networks for smart materials. Proc. Natl. Acad. Sci. USA. 2013; 110:6694–6699. [PubMed: 23569270]

17. Kim D, et al. Dissolvable films of silk fibroin for ultrathin conformal bio-integrated electronics. Nature Mater. 2010; 9:511–517. [PubMed: 20400953]

18. Kim D, et al. Electronic sensor and actuator webs for large-area complex geometry cardiac mapping and therapy. Proc. Natl. Acad. Sci. USA. 2012; 109:19910–19915. [PubMed: 23150574]

19. Yim M, Paik K. The contact resistance and reliability of anisotropically conductive film (ACF). Advanced Packaging, IEEE Transactions on. 1999; 22:166–173.

20. Stieglitz, T. Handbook of Neural Activity Measurement. Brette, R.; Destexhe, A., editors. Cambridge Univ. Press; 2012. p. 8-43.

21. Cogan SF. Neural stimulation and recording electrodes. Annu. Rev. Biomed. Eng. 2008; 10:275–309. [PubMed: 18429704]

22. Cui Y, Wei Q, Park H, Lieber CM. Nanowire nanosensors for highly sensitive and selective detection of biological and chemical species. Science. 2001; 293:1289–1292. [PubMed: 11509722]

23. Bilston, LE. Neural Tissue Biomechanics. Springer; 2011.

24. Hillel AT, et al. Photoactivated composite biomaterial for soft tissue restoration in rodents and in humans. Sci. Transl. Med. 2011; 3:93ra67.

25. Bible E, et al. Attachment of stem cells to scaffold particles for intra-cerebral transplantation. Nature Protoc. 2009; 4:1440–1453. [PubMed: 19798079]

26. Cetin A, Komai S, Eliava M, Seeburg PH, Osten P. Stereotaxic gene delivery in the rodent brain. Nature Protoc. 2006; 1:3166–3173. [PubMed: 17406580]

27. Alvarez-Buylla A, Garcia-Verdugo JM. Neurogenesis in adult subventricular zone. J. Neurosci. 2002; 22:629–634. [PubMed: 11826091]

28. Goldman S. Stem and progenitor cell-based therapy of the human central nervous system. Nature Biotech. 2005; 23:862–871.

29. van Dommelen JAW, van der Sande TPJ, Hrapko M, Peters GWM. Mechanical properties of brain tissue by indentation: Interregional variation. J. Mech. Behav. Biomed. Mater. 2010; 3:158–166. [PubMed: 20129415]

30. Biran R, Martin DC, Tresco PA. Neuronal cell loss accompanies the brain tissue response to chronically implanted silicon microelectrode arrays. Exp. Neurol. 2005; 195:115–126. [PubMed: 16045910]

31. Mercanzini A, et al. Demonstration of cortical recording using novel flexible polymer neural probes. Sens. Acuators, A. 2008; 143:90–96.

32. Symour JP, Kipke DR. Neural probe design for reduced tissue encapsulation in CNS. Biomaterials. 2007; 28:3594–3607. [PubMed: 17517431]

33. Yoshida Kozai TD, et al. Ultrasmall implantable composite microelectrodes with bioactive surfaces for chronic neural interfaces. Nature Mater. 2012; 11:1065–1073. [PubMed: 23142839]

34. Lee H, Bellamkonda RV, Sun W, Levenston ME. Biomechanical analysis of silicon microelectrode-induced strain in the brain. J. Neural Eng. 2005; 2:81–89. [PubMed: 16317231]

35. Navarro X, et al. A critical review of interfaces with the peripheral nervous system for the control of neuroprostheses and hybrid bionic systems. J. Peripher. Nerv. Syst. 2005; 10:229–258. [PubMed: 16221284]

36. Buzsaki G, et al. Hippocampal network patterns of activity in the mouse. Neuroscience. 2003; 116:201–211. [PubMed: 12535953]

37. Agarwal G, et al. Spatially distributed local fields in the hippocampus encode rat position. Science. 2014; 344:626–630. [PubMed: 24812401]

38. Morris G, Arkadir D, Nevet A, Vaadia E, Bergman H. Coincident but distinct messages of midbrain dopamine and striatal tonically active neurons. Neuron. 2004; 43:133–143. [PubMed: 15233923]

39. Zhang J, et al. Integrated device for optical stimulation and spatiotemporal electrical recording of neural activity in light-sensitized brain tissue. J. Neural Eng. 2009; 6

40. Zhou W, et al. Long term stability of nanowire nanoelectronics in physiological environments. Nano Lett. 2014; 14:1614–1619. [PubMed: 24479700]

41. Alivisatos PA, et al. The brain activity map. Science. 2013; 339:1284–1285. [PubMed: 23470729]

42. Almquist BD, Melosh NA. Fusion of biomimetic stealth probes into lipid bilayer cores. Proc. Natl. Acad. Sci. USA. 2010; 107:5815–5820. [PubMed: 20212151]

43. Wise KD, Anderson DJ, Hetke JF, Kipke DR, Najafi K. Wireless implantable microsystems: High-density electronic interfaces to the nervous system. Proc. IEEE. 2004; 92:76–97.

44. Tian B, et al. Three-dimensional, flexible nanoscale field-effect transistors as localized bioprobes. Science. 2010; 329:831–834.

45. Duan X, et al. Intracellular recordings of action potentials by an extracellular nanoscale field-effect transistor. Nature Nanotechnol. 2012; 7:174–179. [PubMed: 22179566]

46. Spira M, et al. Multi-electrode array technologies for neuroscience and cardiology. Nature Nanotechnol. 2013; 8:83–94. [PubMed: 23380931]

47. Tian B, et al. Macroporous nanowire nanoelectronic scaffolds for synthetic tissues. Nature Mater. 2012; 11:986–994. [PubMed: 22922448]

48. Liu J, et al. Multifunctional three-dimensional macroporous nanoelectronic networks for smart materials. Proc. Natl. Acad. Sci. USA. 2013; 110:6694–6699. [PubMed: 23569270]
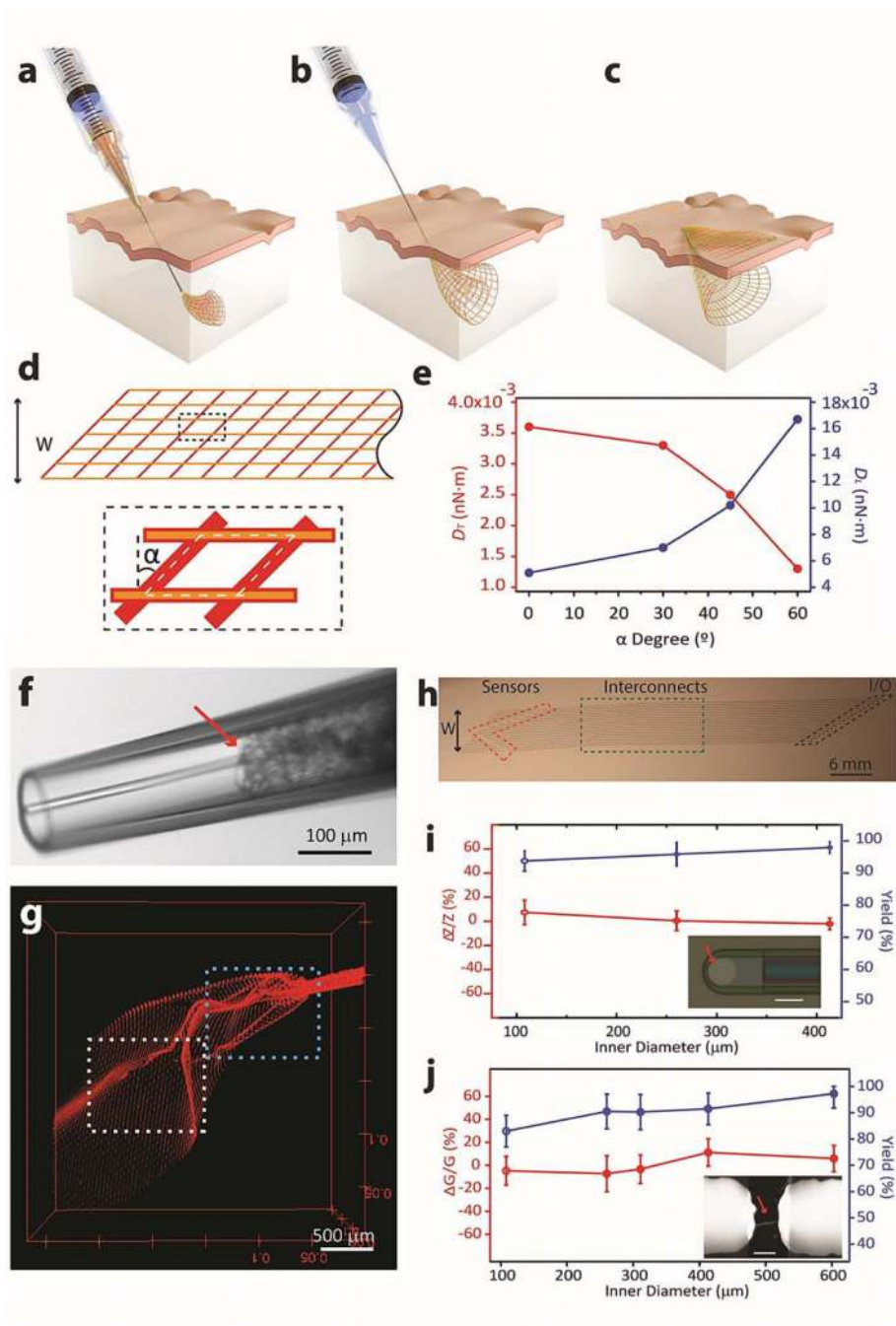
Figure 1. Syringe injectable electronics

a to **c**, Schematics of injectable electronics. The red-orange lines highlight the overall mesh structure and indicate the regions of supporting and passivating polymer mesh layers; the yellow lines indicate metal interconnects between I/O pads (green filled circles) and recording devices (blue filled circles). **d**, Schematic of the mesh electronics design (upper image), where the orange and red lines represent polymer encapsulated metal interconnects and supporting polymer elements, respectively, and *W* is the total width of the mesh. The dashed black box (lower image) highlights the structure of one unit cell (white dashed lines),

where a is the angle deviation from rectangular. **e**, Longitudinal mesh bending stiffness, D_L, and transverse mesh bending stiffness, D_T, as a function of a defined in **d**. **f** and **g**, Images of mesh electronics injection through a glass needle, ID = 95 μm, into 1x PBS solution. Bright-field microscopy image **f** of the mesh electronics immediately prior to injection into solution; the red arrow indicates the end of the mesh inside the glass needle. 3D reconstructed confocal fluorescence image **g** recorded following injection of ca. 0.5 cm mesh electronics into 1x PBS solution. The blue and white dashed boxes correspond to regions shown in Supplementary Fig. 3a and b. **h**, Optical image of an injectable mesh electronics structure unfolded on a glass substrate. *W* is the total width of the mesh electronics. The red dashed polygon highlights the position of electrochemical devices or FET devices. Green and black dashed boxes highlighted metal interconnect lines and metal I/O pads, respectively. **i** and **j**, Yields and change with ±1 standard deviation (±1SD) in properties post-injection for single-terminal electrochemical and two-terminal field-effect transistor (FET) devices. **i**, Yield (blue) and impedance change (red) of the metal electrodes from the mesh electronics injected through 32, 26 and 22 gauge metal needles. Inset: bright field image of a representative metal electrode on mesh electronics, where the sensing electrode is highlighted by a red arrow. Scale Bar: 20 μm. **j**, Yield (blue) and conductance change (red) of silicon nanowire FETs following injection through 32, 26, 24, 22 and 20 gauge needles. Inset: scanning electron microscopy (SEM) image of a representative nanowire FET device in the mesh electronics; the nanowire is highlighted by the red arrow. Scale bar: 2 μm.
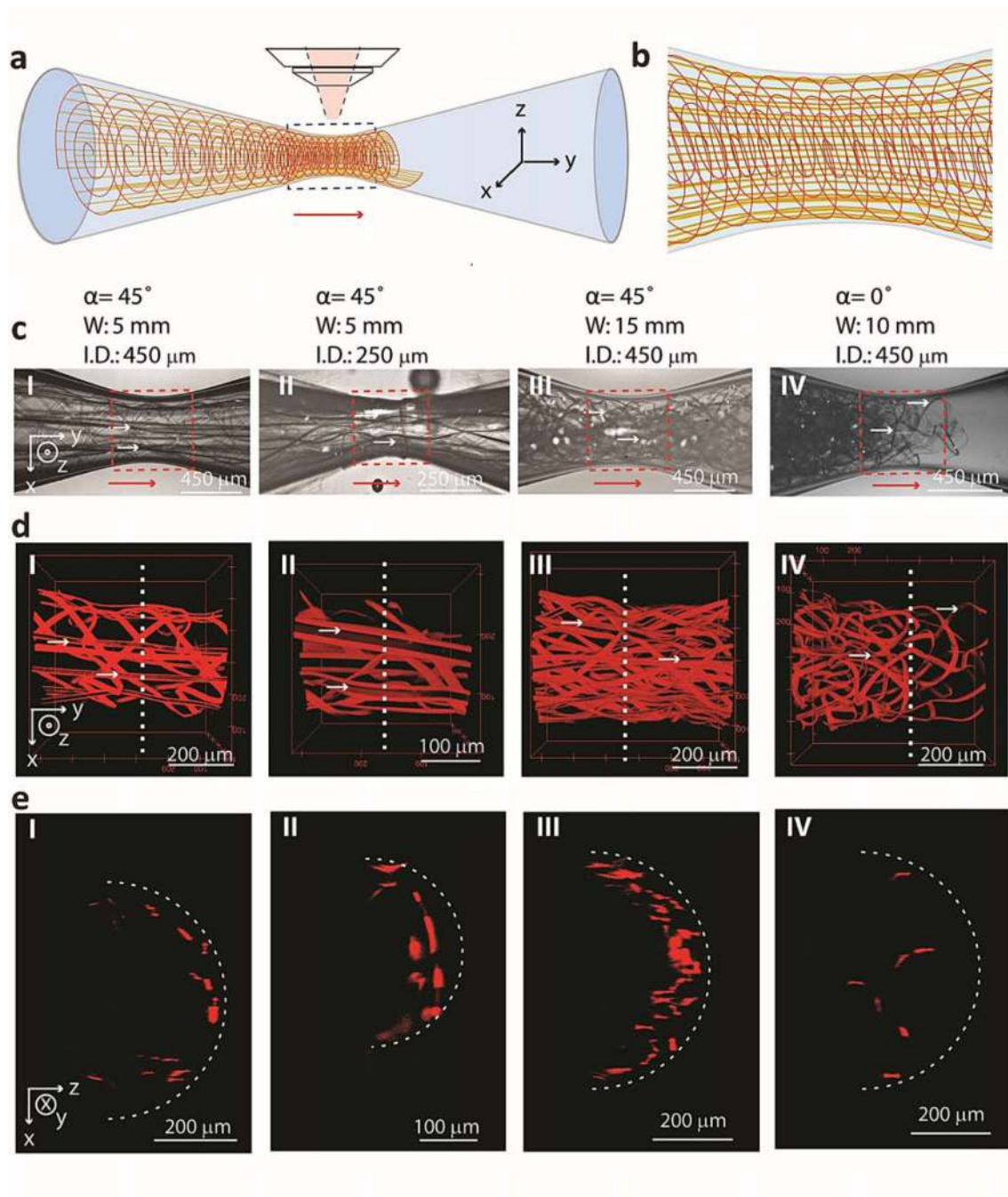
Figure 2. Imaging mesh electronics structure in needle constrictions

a, Schematic illustrating the structure of a pulled glass tube (blue) with mesh electronics passing from larger (left) to smallest (center) ID of tube, where the red arrow indicates the direction of injection and x-y-z axes indicate coordinates relative to the microscope objective for images in **c** to **e**. **b**, Schematic image of the mesh structure from the region of the constriction indicated by the blue dashed box in **a**. **c**, Bright-field microscopy images of different design mesh electronics injected through glass channels. **I** and **II**, total width, $W =$ 5 mm, $\alpha = 45°$ mesh electronics injected through 450 and 250 µm ID, respectively, glass

channels. **III**, $W = 15$ mm, $a = 45°$ mesh electronics injected through a 450 μm ID glass channel. **IV**, $W = 10$ mm, $a = 0°$ mesh electronics injected through a 450 μm ID glass channel. The injection direction is indicated by red arrows in the images; the orientation relative to the axes in **a** are indicated in **I** and the same for panels **I** to **IV**. **d**, 3D reconstructed confocal images from the dashed red box regions in the respective panels **I** to **IV** in **c**; the x-y-z axes in **I** are the same for panels **II** to **IV**. Horizontal, small white arrows in **c** and **d** indicate several of the longitudinal elements containing metal interconnects in the mesh electronics. **e**, Cross-sectional images plotted as half cylinders from positions indicated by the vertical white dashed lines in **d**. The white dashed curves indicate the approximate IDs of the glass constrictions.
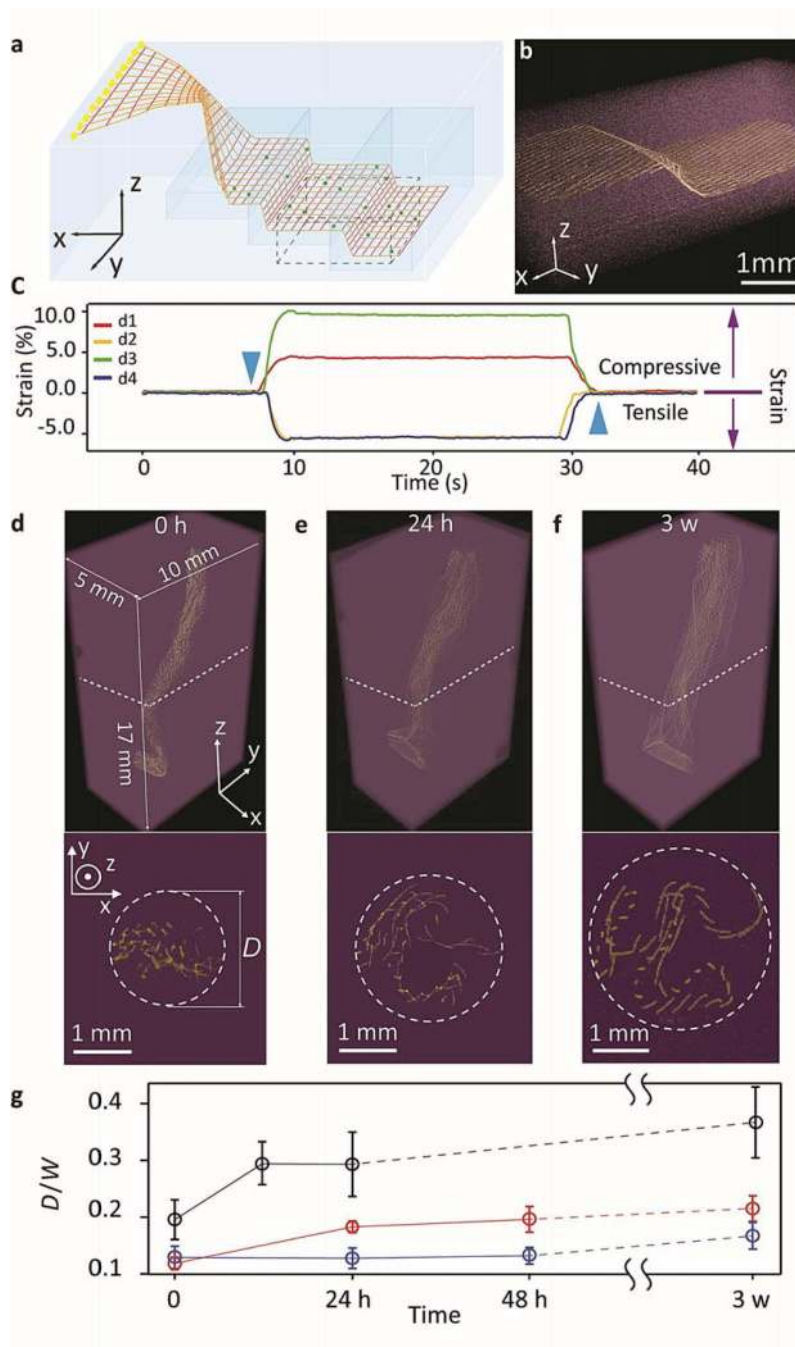
Figure 3. Syringe injection of mesh electronics into 3D synthetic structures
a, Schematic of a mesh electronics injected with uncured PDMS precursor into a PDMS cavity (blue) with I/O pads unfolded outside the cavity. The injected PDMS precursors were cured after injection. The red lines highlight the overall mesh structure and indicate the regions of supporting and passivating polymers and the yellow lines indicate the metal interconnects between I/O pads (yellow filled circle) and devices (dark blue filled circle). **b**, μCT image shows the zoomed-in structure highlighted by the black dashed box in **a** and Supplementary Fig. 7b. False colors were applied with metal lines (yellow) in PDMS

(purple). **c**, 4 nanowire devices response to pressure applied on the PDMS. The blue downward and upward pointing triangles denote the times when the strain was applied and released, respectively. The purple downward and upward arrows show the tensile and compressive strains, corresponding to the minus and plus change of conductance, respectively. **d** to **f**, (upper images) 3D reconstructed μCT images of a mesh electronics injected into 75% Matrigel™ after incubating for 0 h **d**, 24 h **e**, and 3 weeks **f** at 37 °C. The x-y-z axes are shown in **d** and the same for panels **e** and **f**, where the injection direction is ca. along the z-axis. In **d** to **f**, false colors were applied with metal lines in the mesh (yellow) and the Matrigel™ (purple) (lower images). Corresponding cross-section images at z = 10 mm with 500 μm thicknesses; the positions of the cross-sections are indicated by white dashed lines in the upper images. The maximum extent of mesh electronics unfolding was highlighted by white dashed circles with diameter, *D*, in each image. **g**, Time dependence of mesh electronics unfolding following injection into 25% (black), 75% (red) and 100% (blue) Matrigel™; the measured diameter, *D*, was normalized by the 2D width, *W*, of the fabricated mesh electronics. *D* was sampled from five cross-sections taken at z =5, 7.5, 10, 12.5 and 15 mm to obtain the average ± 1SD.
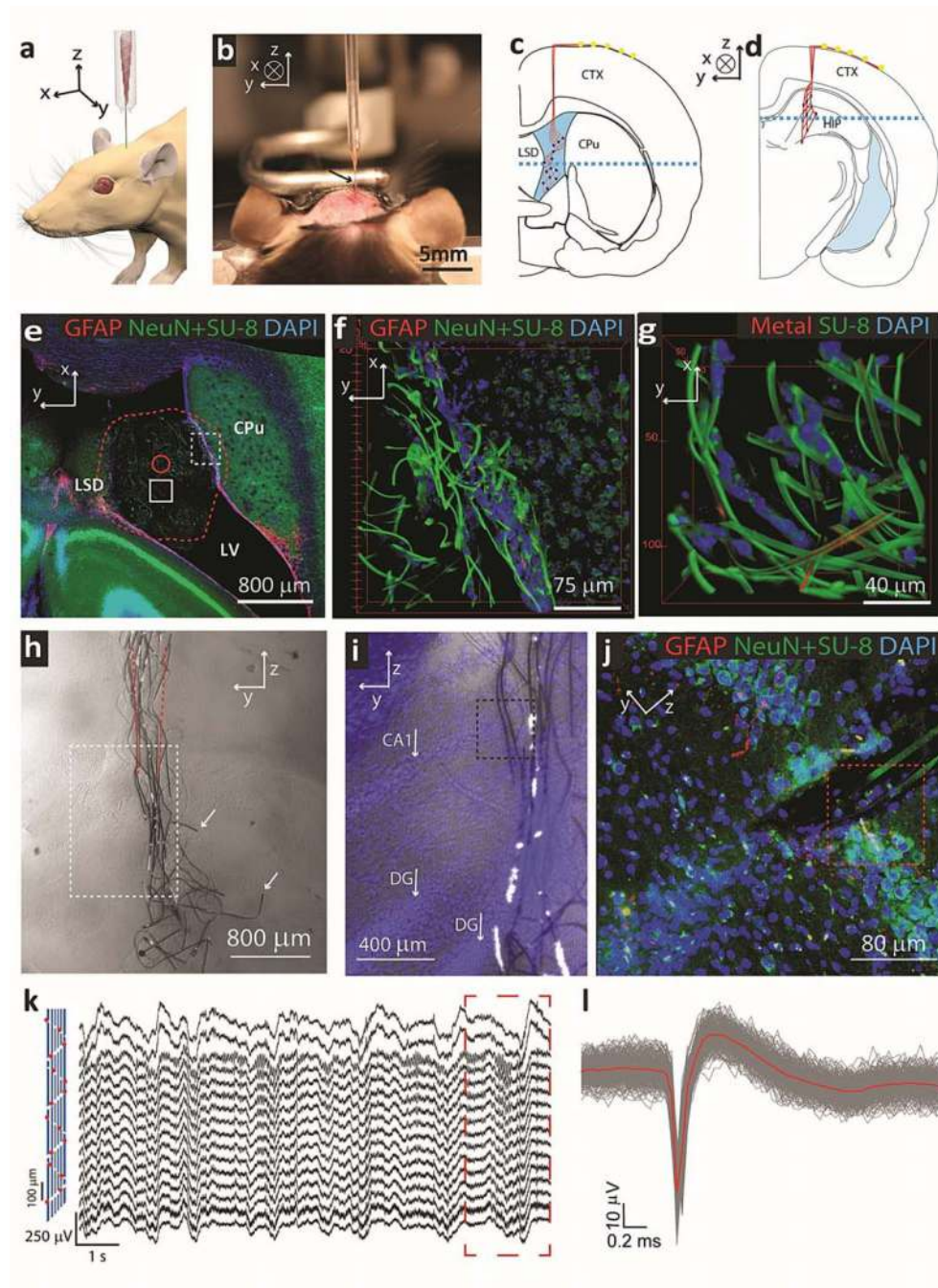
Figure 4. Syringe injectable electronics into *in vivo* biological system
a, Schematic shows *in vivo* stereotaxic injection of mesh electronics into a mouse brain. **b**, Optical image of the stereotaxic injection of mesh electronics into an anesthetized 3 months old mouse brain. **c** and **d**, Schematics of coronal slices illustrating the two distinct areas of the brain that mesh electronics were injected: **c**, through the cerebral cortex (CTX) into the lateral ventricle (LV) cavity adjacent to the caudoputamen (CPu) and lateral septal nucleus (LSD), and **d**, through the CTX into the hippocampus (HIP). Red lines highlight and indicate the overall structure of mesh and dark blue filled circles indicate recording devices.

The blue dashed line in **c** indicates the direction of horizontal slicing for imaging. **e**, Projection of 3D reconstructed confocal image from 100 μm thick, 3.17 mm long and 3.17 mm wide volume horizontal slice 5 weeks post-injection at the position indicated by blue dashed line in **c**. Red dashed line highlights the boundary of mesh inside LV, and the solid red circle indicates the size of the needle used for injection. The red, green and blue colors in this correspond to GFAP, NeuN/SU-8 and DAPI, respectively, and are denoted at the top of the image panel in this and subsequent images. **f**, 3D reconstructed confocal image from the dashed red box in Supplementary Fig. 8a at the interface between mesh electronics and subventricular zone (SVZ). **g**, 3D reconstructed confocal image from dashed red box in Supplementary Fig. 8c at the ca. middle (of x-y plane) of the LV in the slice. **h**, Bright-field microscopy image of a coronal slice of the HIP region 5 weeks post-injection of the mesh electronics at the position indicated in schematic **d**. Red dashed lines indicate the boundary of the glass needle. The white arrows indicate longitudinal elements that were broken during tissue slicing. Black dashed lines indicate the boundary of each individual image. **i**, Overlaid bright field and epi-fluorescence images from the region indicated by white dashed box in **h**. Blue corresponds to DAPI staining of cell nuclei, white arrows indicate CA1 and dentate gyrus (DG) of the HIP. **j**, Projection of 3D reconstructed confocal image from 30 μm thick, 317 μm long and 317 μm wide volume from the zoomed-in region highlighted by the black dashed box in **i**. **k**, Acute *in vivo* 16-channel recording using mesh electronics injected into a mouse brain. The devices were Pt-metal electrodes (impedance ~950 kΩ at 1 kHz) with their relative positions marked by red spots in the schematic (left panel), and the signal was filtered with 60 Hz notch during acquisition. The dashed red rectangle indicates the part for spatiotemporal mapping of multichannel-LFP recordings (Supplementary Fig. 12d) **l**, Superimposed single-unit neural recordings from one channel after 300-6000 Hz band-pass filtering. The red line represents the mean waveform for the single-unit spikes.